

Session MT-1

Modeling and Testing(1)

The Effect of Ultrasonic Power on Bonding Pad and IMD Layers in Ultrasonic Wire Bonding

Insu JEON, Qwanho CHUNG, Joonki HONG, Kwangyoo BYUN, Hynix Semiconductors Inc, Korea

The Mechanical and Electrical Properties of 6.5 Wt.% Si Steel for Advanced Electric Components

Young-Ki YOON, Jin-Hyeok KIM, Hi-Seak YOON, Chonnam National University, Korea

Circuit Modeling Technique of Electrical Package Considering S-Parameters Measurement Environments

Yong-Ju KIM, Young-Suk SUH, Hwa-Jung KIM, Hynix Semiconductors, Korea
Kwang-Seong CHOI, Electronics and Telecommunications Research Institute, Korea

The Effect of Ultrasonic Power on Bonding Pad and IMD Layers in Ultrasonic Wire Bonding

Insu Jeon, Qwanho Chung, Joonki Hong, and Kwangyoo Byun
PKG & Module R&D, Semiconductor Manufacturing Division, Hynix Semiconductor Inc.
San 136-1, Ami-ri, Bubal-eub, Ichon-si, Kyoungki-do, 467-791, Korea
jis@hynix.com, qhchung@hynix.com, joonki.hong@hynix.com and bkyo@hynix.com

Abstract

The effect of ultrasonic power on the reliability of bonding pad and IMD(Inter Metallic Dielectric) layers has been investigated with numerical analysis and experimental survey. Such a reliability can be characterized by maximum equivalent plastic strain in bonding pad and maximum Mises stress in IMD layers. The whole process of ultrasonic wire bonding is simulated by the finite element method to study the characteristics of ultrasonic power. From the results of this study, we find that the ultrasonic power is closely related to the surface crack on bonding pad as well as the fracture of IMD layers.

Introduction

In ultrasonic wire bonding, it is known that four main bonding parameters, that is, ultrasonic power, bonding force, time and heater block temperature are influencing factors on the bondability and the bond reliability by many researches [1, 2, 3, 4]. The effect of these bonding parameters on bond shear strength was investigated by Guzman and Mahaney[1] and Hu et al.[2]. They have found that the ultrasonic power is a dominant variable in ball formation and has a critical effect on the bond shear strength. Liang et al.[3] and Shu[4] have made a lot of effort to optimize the bonding parameters in order to improve the bondability characterized by ball shear stress and the ball bond reliability that can be determined by in-situ ball bond degradation measurement. Particularly, Liang et al.[3] introduced a concept of 'reduced bonding parameter' and they were able to relate the bonding parameters directly to bondability and ball bond reliability.

However the research about the immediate effect of ultrasonic power on bonding pad or on IMD layers in chip is not shown in this field until these days, as far as we know. Therefore a complete understanding of the effect of ultrasonic power upon bonding pad and IMD layers is necessary in order to handle the wire bonding failure which stems from the chip itself like bond pad metal peeling[5, 6].

Several numerical analyses of wire bonding process have been carried out for understanding the bonding mechanism. Among these works, Chidambaram[7] evaluated the gold wire fatigue parameters and the 'Mean Time To Failure' using temperature cycle data in conjunction with the strains obtained from finite element analysis. Moreover, Takahasi et al.[8] simulated wire deformation processes during thermo-compression bonding without ultrasonic vibration using finite element technique. The finite element simulation of the wire looping process in ball-wedge wire bonding was studied by Tay et al.[9]. They compared the obtained resultant wire bonding profiles with actual samples. Recently, Takahasi et al.[10, 11] published two papers about numerical analysis of

fine lead bonding. They reported the effect of pad thickness and pad mechanical properties on inner lead bonding considering the viscoplastic behavior of lead and pad.

In this paper we focus on the 'mechanical' effect of ultrasonic power on the reliability of bonding pad and IMD layers ignoring the chemical reaction between Al bonding pad and Au wire ball(air free ball), namely, the diffusion phenomenon between these two materials. Under the assumption of elastic-plastic behavior of bonding pad and elastic behavior of IMD layers, the reliability can be characterized by the maximum equivalent plastic strain in bonding pad and the maximum Mises stress in IMD layers.

Characterization of ultrasonic wire bonding problem

The ultrasonic wire bonding process is composed of various mechanical, thermal and chemical problems, such as dynamic load transfer, mechanical and thermal contact, friction, transient heat transfer problem, and diffusion problem between Au wire ball and Al bond pad.

In this study, the dynamic behavior of capillary and wire ball is replaced with the behavior without mass effect because we have interest in the deformation of wire ball the mass of wire ball of which mass is very small. Furthermore, for the sake of simplicity in numerical analysis, we ignore the chemical reaction between bonding pad and wire ball.

However, we choose the mechanical contact problem with friction in order to compensate for the bonding strength during the wire bonding process. For the large deformation of wire ball and bonding pad, we utilize the non-linear finite element method for the geometry and material non-linearity of each material. The thermal contact and the transient heat transfer problems are also considered. The thermal contact problem has been investigated by many researchers in the last sixty years. Much published theoretical and experimental work has been devoted to problems related to thermal contact conductance. Several notable researches have been published along this line[12-15]. Especially, Tseng[16, 17] has studied more practical application with the thermal contact conductance. He analyzed the rolling process taking into account the thermal contact conductance using finite element method.

Governing equations for mechanical contact problem

Consider two bodies that are contacting mechanically and thermally with each other under plane strain deformation shown in Fig. 1.

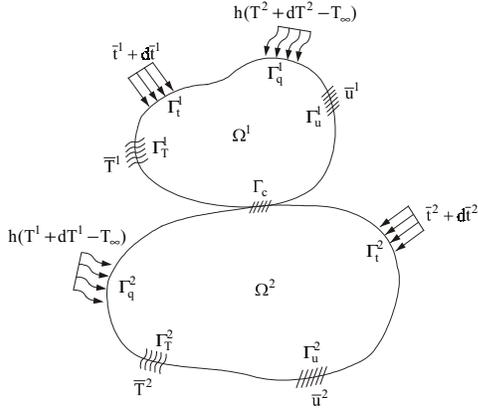


Fig. 1 Two bodies in contact with mechanical and thermal boundary condition

We assume that the material property of two bodies is isotropic, and that each boundary of two bodies contains five types of boundary condition. The displacement and the traction boundary conditions are prescribed in Γ_u and Γ_t , the temperature and the convection boundary conditions are given in Γ_T and Γ_q . Moreover Γ_c denotes the part of boundary where contacts may occur. It is also assumed that the heat transfer by radiation is neglected.

Then in the absence of the body forces the equilibrium equation is written as

$$(\sigma_{ij} + d\sigma_{ij})_{,j}^k = 0 \quad \text{in } \Omega^k \quad (1)$$

where superscript 'k' denotes body numbering and the comma indicates partial differentiation with respect to the Cartesian coordinate x_i . When the traction applied on the boundary increases, the plastic deformation will occur. For the plastic zone, the constitutive equations in incremental form[18, 19] for thermal elastic-plastic material[20] will be derived as follows

$$d\sigma_{ij} = 2G(d\varepsilon_{ij} + \frac{\nu}{1-2\nu}\delta_{ij}d\varepsilon_{ll}) - \frac{3Gs_{kl}d\varepsilon_{kl}s_{ij}}{\sigma_e^2(1+H/3G)} + \frac{(\partial\sigma_Y/\partial T)dT}{\sigma_e(1+H/3G)}s_{ij} - 2K\delta_{ij}d\varepsilon^T \quad (2)$$

In case of elastic conditions, the change in stress $d\sigma_{ij}$ can be written as

$$d\sigma_{ij} = 2G(d\varepsilon_{ij} + \frac{\nu}{1-2\nu}\delta_{ij}d\varepsilon_{ll}) - 2K\delta_{ij}d\varepsilon^T \quad (3)$$

where T is the temperature, G is the shear modulus, ν is the Poisson's ratio and K is the bulk modulus of the material. Moreover, $H = \partial\sigma_Y/\partial\varepsilon^p$ is the hardening modulus, σ_Y is the yield stress, s_{ij} is the stress deviator, σ_e is the effective stress and ε^T is the uniaxial thermal dilatation for the material.

For the concise expression of the equations (2) and (3), the superscript 'k' which refers the body numbering is omitted.

The strain-displacement relations are

$$d\varepsilon_{ij} = \frac{1}{2}(du_{i,j} + du_{j,i}) \quad (4)$$

The mechanical boundary conditions are expressed as follows

$$u_i = \bar{u}_i \quad \text{on } \Gamma_u^k \quad (5)$$

$$(\sigma_{ij} + d\sigma_{ij})^k n_j^k = \bar{t}_i^k + d\bar{t}_i^k \quad \text{on } \Gamma_t^k \quad (6)$$

where \bar{u}_i , n_j and \bar{t}_i are the prescribed displacement, the unit normal vector and the traction on each boundary, respectively.

The mechanical contact conditions can be represented as

$$p = 0 \quad \text{on } \Gamma_c \quad (7)$$

$$f_i \leq 0, \quad f_2 \leq \mu f_1 \quad \text{on } \Gamma_c \quad (8)$$

For the contact boundary, the penetration between each body is denoted by P . Therefore, $p = 0$ means the non-penetration condition for the contact problem. The contact traction component and the friction coefficient are denoted by f_i and μ , respectively.

Governing equations for thermal contact problem

In Fig.1, two bodies are thermally contacted with each other. The heat of each body transfers to the atmosphere and is exchanged with each other. In this case, the heat transfer in transient state has to be considered. The governing equation of the transient heat transfer can be written as

$$(q_i + dq_i)_{,i}^k = \rho^k c_p^k \frac{\partial(T + dT)}{\partial t} \quad \text{in } \Omega^k \quad (9)$$

$$dq_i^k = -\kappa^k T_{,i} \quad (10)$$

where ρ is the density, c_p is the specific heat, κ is the coefficient of thermal conductivity, the q_i is the heat flux component and dT is the temperature change during a load increment.

The initial boundary condition is expressed as follows

$$T|_{t=0} = T_0 \quad (11)$$

The thermal boundary conditions are expressed as

$$T = \bar{T} \quad \text{on } \Gamma_T^k \quad (12)$$

$$(q_i + dq_i)^k n_i^k = h[(T + dT) - T_\infty] \quad \text{on } \Gamma_q^k \quad (13)$$

where T_0 is the initial temperature of each body, \bar{T} is the prescribed temperature on Γ_T , T_∞ is the temperature of the atmosphere and h is the convection coefficient.

The thermal contact condition is expressed as follows

$$(q_i + dq_i)^k n_i^k = h_c [(T_i + dT_i)_b - (T_j + dT_j)_b] \quad \text{on } \Gamma_c \quad (14)$$

where T_i and T_j are the temperatures of two bodies contacted with each other. The subscript 'b' represents the boundary of contact surface. Moreover h_c is the thermal contact conductance, which can be divided into three terms as follows(Tseng[16, 17]),

$$h_c = h_{cs} + h_{cm} + h_{cr} \quad (15)$$

where h_{cs} , h_{cm} and h_{cr} are the conductance components of solid, fluid medium and radiation, respectively. The expressions of each component will be shown in Appendix A.

Finite element formulation

The finite element formulation for the mechanical contact problem can be developed using the equations (1)-(8) and the principle of virtual work for mechanical problem which is written as

$$\int_V (\sigma_{ij} + d\sigma_{ij})_{,j} \delta u_i dV = 0 \quad (16)$$

Besides, for the case of the thermal contact problem, the equations (9)-(15) and the variational equation for transient heat transfer equation (17) can be utilized.

$$\int_V [(q_i + dq_i)_{,i} - \rho c_p \frac{\partial(T + dT)}{\partial t}] \delta T dV = 0 \quad (17)$$

For the sake of simplicity in notation, the superscript 'k' is omitted in the equations (16) and (17).

After obtaining the matrix equations for the mechanical and thermal contact problem from the variational equations (16) and (17), two matrix equations may be combined with each other to find the mechanical and thermal solutions, simultaneously. For more detailed procedure of the finite element formulation, see the work of Park and Kwak[21].

In this paper, we use the package code ABAQUS for the finite element solution. ABAQUS uses the penalty method or Lagrangian multiplier method for the mechanical contact problem and offers the analysis technique related to the thermal contact problem.

Material properties for numerical examples

The capillary and the wire as well as wire ball are usually made of the materials such as Al_2O_3 and 99.9% Au, respectively. The components of chip such as bonding pad, IMD layers and active die are also made from Al, SiO_2 species and Si, respectively. For numerical analysis, the representative

material properties of each material depending upon the temperature are chosen from the material handbooks[22-24]. However, the elastic modulus and the yield stress of gold wire depending on temperature are taken from the experimental results. These results will be shown in Appendix B. For the elastic-plastic calculation based on the incremental plasticity (2) and (3) is processed with a power-law hardening rule of the form (Mcmeeking[18] and Jeon and Im[19])

$$\frac{\bar{\epsilon}^p}{\epsilon_Y} = \alpha \left(\frac{\bar{\sigma}}{\sigma_Y} \right)^m \quad (18)$$

where $\bar{\epsilon}^p$ is the equivalent plastic strain, $\epsilon_Y = \sigma_Y / E$ is a reference strain component; $\bar{\sigma}$ is the Mises stress, α is the non-dimensional parameter, m is the power-law hardening exponent, typically $m=1$ is the linear elastic and $m=\infty$ is the perfectly plastic. We choose $\alpha=1$ and $m=12$ for numerical computation. The isoparametric plane strain element with eight nodes is adopted for modeling. We choose the selective reduced integration scheme to prevent the excessive incompressible constraint in elastic-plastic deformations.

Finite element mesh and initial boundary conditions

The finite element meshes for capillary, wire and wire ball are presented in Fig. 2. The geometry data for the capillary are taken from its design drawing. In order to save the computation time, we choose the total length of wire to be 1240 μ m. The diameter of wire ball, which is formed by EFO(Electric Flame Off) electrode, is empirically known as 2.5~3 times that of gold wire, so we set it to be 60.96 μ m. The mesh structure of chip is shown in Fig. 3. The geometry data of the chip including bonding pad and various kinds of IMD layers are taken from the measured data of real chip.

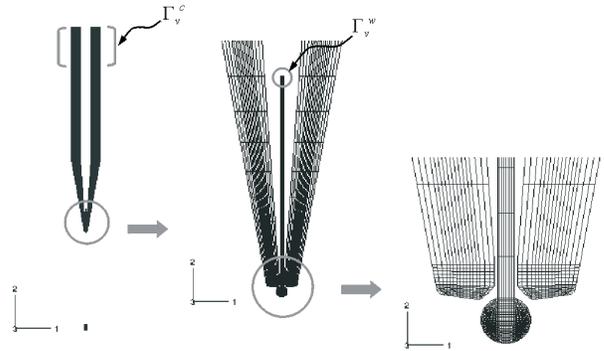


Fig. 2 The finite element mesh shape of the capillary, wire and wire ball

For initial temperature boundary condition, the absolute scale temperature 298.15K for capillary and chip is selected. Moreover, for wire and wire ball, the measured value 1413.75K is also selected to consider the transient heat transfer during the wire bonding process.

Boundary condition for mechanical solution

For the displacement boundary condition, x-direction degree of freedom is fixed to the nodes on the outside of

capillary. To prevent the rigid body motion of the wire and wire ball, x-direction degree of freedom of several nodes near the end of wire is also fixed. The symmetry boundary condition is applied to the left and right side of chip. Furthermore, the y-direction degree of freedom of the nodes on the bottom of chip is fixed.

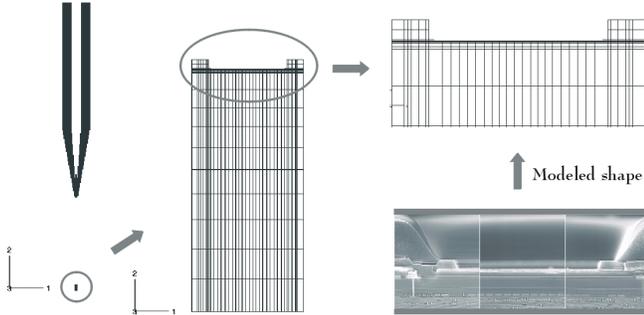


Fig. 3 The finite element mesh shape of chip and the cross-section SEM image of real chip

The major driving force in wire bonding process stems from the motion of capillary. Therefore the reasonable description of the whole motion of capillary as a boundary condition is the key to the numerical analysis of wire bonding. As the displacement boundary condition applied to the capillary, we select 4 types of its behavior as follows; the vertical descent, the vertical compression to the wire ball, the horizontal vibration and the vertical ascent. Among these behavior, the vertical descent and the vertical compression stand for the bonding force and the horizontal vibration represents the ultrasonic power.

For the vertical descent we apply the y-direction displacement to Γ_v^c on capillary surface and to Γ_v^w on wire surface(see Fig. 2) in 3msec until the lower surface of the wire ball contacts with the bonding pad and the upper one contacts with the tip of capillary, simultaneously. After then we set the y-direction displacement of capillary to be $-36.2\mu\text{m}$, which means the 50gf of bonding force, in 30msec for the vertical compression preventing the rigid body motion. After the termination of the vertical compression process, the horizontal vibration is applied along the x-direction to the outside of capillary but the capillary still maintains the same y-direction position, $-36.2\mu\text{m}$. The amplitude and the frequency of the vibration are chosen as $2\mu\text{m}$, which means the 60mW of the ultrasonic power, and 125KHz, respectively. Although the actual vibration time is about 5~15msec, to save the computation time, only 0.008msec that accord with the 1 cycle of the vibration is applied to the capillary. Finally, for the vertical ascent, we apply the displacement of positive y-direction to the Γ_v^c on the capillary surface as $29\mu\text{m}$ in 20msec.

Note that all aforementioned values for displacement boundary conditions are collected from the measured and empirically known data of wire bonding process.

Boundary condition for thermal solution

Because of the selected heater block temperature of bonding machine, the bottom of chip always maintains

constant temperature, 503.15K during the wire bonding process. Therefore we apply the temperature boundary condition to the nodes at the bottom of chip to be 503.15K. Then we consider the transient heat conduction from the bottom to the top surface of chip.

The convection boundary condition is applied on the outside of capillary, the surface of wire ball and the top surface of chip. During the behaviors of the capillary except the vertical descent, we consider that all surfaces are exposed to the natural convection. Hence we select $h = 15W / m^2 K$ as the convection coefficient for those surfaces. For the vertical descent process of the capillary, however, the convection coefficients are selected as $h = 635.9W / m^2 K$ for the surface of the wire ball and $h = 52.38W / m^2 K$ for the outside of capillary.

In order to obtain these coefficients, we assume that the surface of the wire ball is a 1m-long cylinder and the outside of the capillary is a 1m-wide plate. Then we utilize the measured velocity of capillary, which is 2m/sec, and the non-dimensional numbers, i.e., Nusselt number, Reynolds number and Prandtl number to calculate these coefficients.

Numerical results and discussions

The deformation results for the whole wire bonding process are shown in Figs. 4 and 5. The status of the capillary after vertical descent is presented in Fig. 4. Fig. 4 shows that the tip of capillary contacts with the upper surface of wire ball and the lower surface of wire ball contacts with the bonding pad, simultaneously.

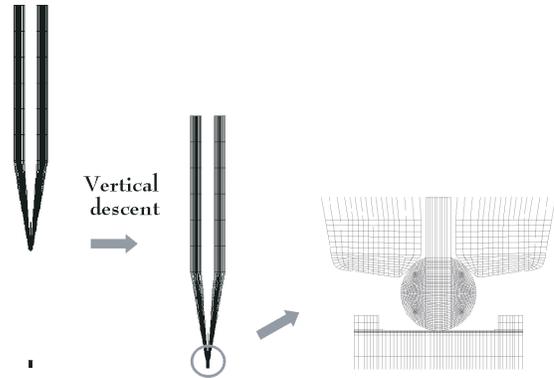


Fig. 4 The vertical descent of the capillary

In Fig. 5, the deformed shapes of wire ball and bonding pad after the vertical compression, horizontal vibration and vertical ascent are shown. From this figure, we see that plastic deformation is occurred in wire ball during the vertical compression of capillary, and that the shape around the ball neck is highly affected by the inner shape of its tip. Furthermore, we find a significant fact that the bonding pad is experienced severe deformation by wire ball during the horizontal vibration. Because the shearing load induced by capillary transmits to bonding pad through wire ball, the shearing deformation of bonding pad can be occurred.

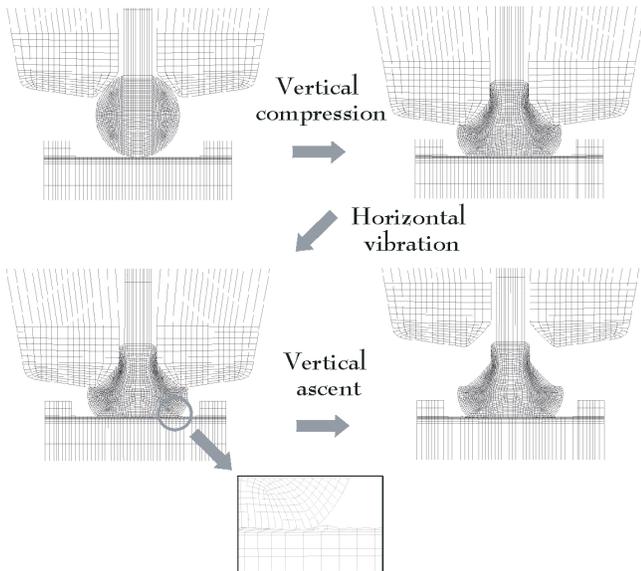


Fig. 5 The deformed shapes of wire ball and bonding pad during wire bonding process

The x-direction displacement boundary condition applied to the outside of capillary versus increasing time for the horizontal vibration is presented in Fig. 6.

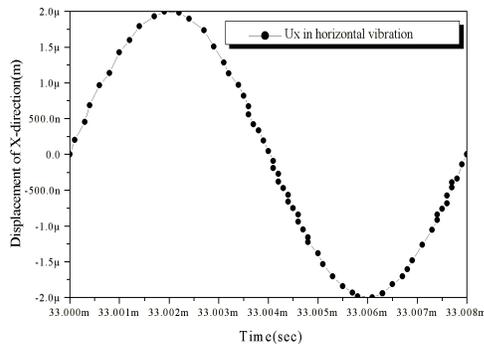


Fig. 6 The x-direction displacement of capillary during the horizontal vibration

The two deformed shapes of wire ball obtained from the numerical analysis and from the actual manufacturing process are presented in Fig. 7.

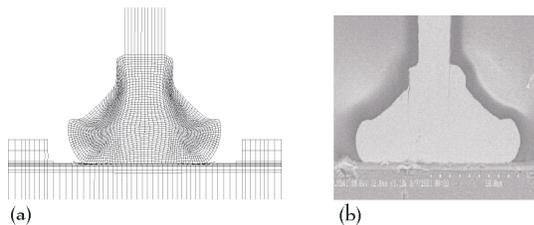


Fig. 7 The deformed shape of the wire ball obtained from (a) numerical analysis and (b) actual manufacturing process

Fig. 7(b) is the SEM image of cross section of the actual wire ball. The same bonding conditions are used for comparing their results with each other. Even though there are some differences in geometry as well as material data between the

modeled and the actual wire bonding process, Fig. 7 shows a good agreement between these two deformed shapes.

The temperature change of the wire ball and bonding pad versus increasing time during wire bonding process is shown in Fig. 8. For obtaining those temperatures, we select two points from each body, where the mechanical contact is initiated between the pad and the wire ball.

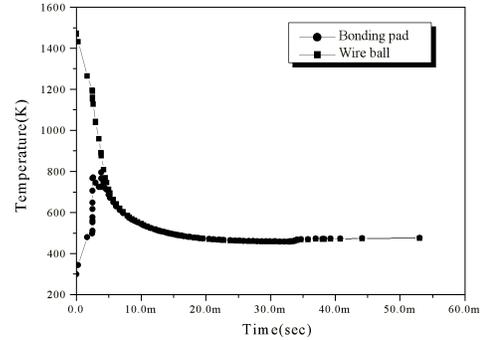


Fig. 8 The temperature of wire ball and bonding pad during wire bonding process

From Fig. 8, we see that the temperature of wire ball is rapidly decreased during the vertical descent and the early stage of vertical compression. Moreover the wire ball increases the temperature of bonding pad rapidly when the contact between each body begins. After then, the temperature of wire ball and bonding pad decreases together. From this results, we find that the temperature of wire ball and bonding pad is affected by the temperature of heater block while the wire ball is deformed and vibrated.

Because we find the fact that the deformation of bonding pad during the horizontal vibration is severe from Fig. 5, we attempt to investigate the equivalent plastic strain and the Mises stress in chip. The distribution of equivalent plastic strain and Mises stress around wire ball is presented in Fig. 9 when the maximum value of equivalent plastic strain and the maximum Mises stress in the chip are computed during wire bonding process.

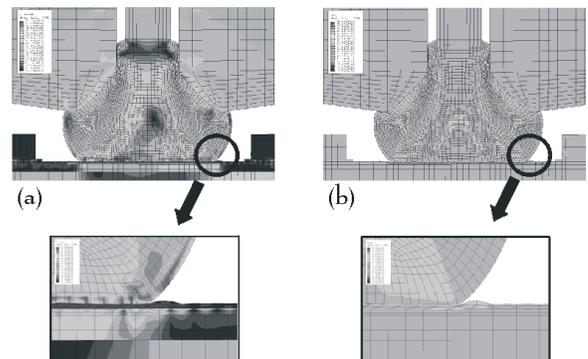


Fig. 9 The distribution of (a) equivalent plastic strain and (b) Mises stress during the wire bonding process

From Fig. 9, we find that it is the horizontal vibration to make the maximum value of equivalent plastic strain and the maximum Mises stress. The region where these values are calculated are bonding pad and IMD layer underneath the pad,

respectively. The horizontal vibration of capillary transmits the shearing load to bonding pad through wire ball, and the transmitted shearing load increases the equivalent plastic strain in bonding pad. Although the pad contacts with the wire ball and the compression load as well as the shearing load are transmitted directly to it, less stress is computed in bonding pad than in IMD layer underneath the pad because of its elastic-plastic behavior.

The change of equivalent plastic strain in bonding pad and Mises stress in IMD layer underneath the pad during wire bonding process is shown in Fig. 10.

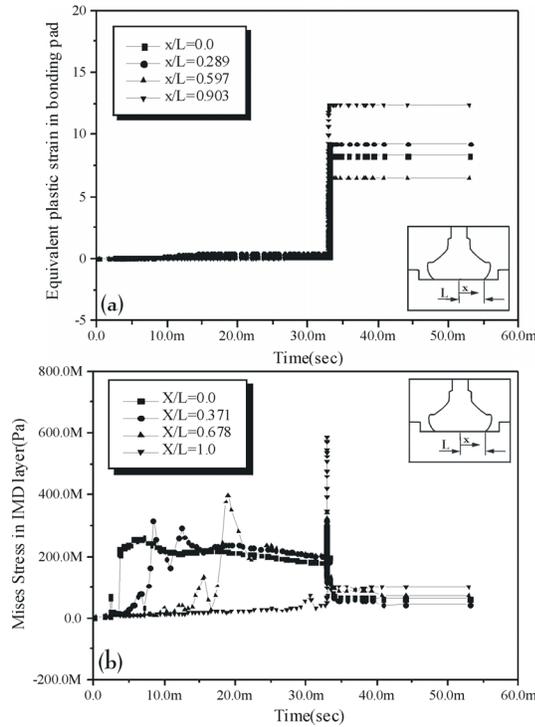


Fig. 10 (a) The equivalent plastic strain in bonding pad and (b) The Mises stress in IMD layer versus increasing time

Especially, Fig. 10(a) shows that the maximum value of equivalent plastic strain takes place in bonding pad underneath the edge of deformed wire ball ($x/L = 0.903$). Because the equivalent plastic strain is closely related to fracture or failure of a metal, the severe equivalent plastic strain in Fig. 10 explains that the possibility of initiation of surface crack on the pad underneath the edge of deformed wire ball is very high.

Fig. 10(b) shows that the maximum value of Mises stress is also taken place in IMD layer beneath the edge of deformed wire ball ($x/L = 1.0$). Besides, it shows that the shearing load have more serious effect on IMD layers than the compression load, because the compression load is transferred from 3msec to 33msec. Such stress that mainly depends upon the shearing load is expected to make a significant effect on the fracture of IMD layers and on the propagation of the surface crack into the IMD layers.

In fact, those values in Fig. 10 are overestimated because we have assumed the infinite friction coefficient between wire ball and bonding pad. However, the actual trend of increasing equivalent plastic strain in bonding pad and Mises stress in the

IMD layer will be similar to these results because of the bonding strength between the pad and the wire ball.

Fig. 11(a) shows the actual surface cracks on bonding pad after the regular wire bonding process. From Fig. 11(a) we find that the surface crack is located around the edge of deformed wire ball. This figure shows an excellent agreement with the result of Fig. 10(a). To find these surface cracks, we try the PCT(Pad Cratering Test), which enables us to remove the deformed wire ball after the bonding process without any scratch of the pad surface.

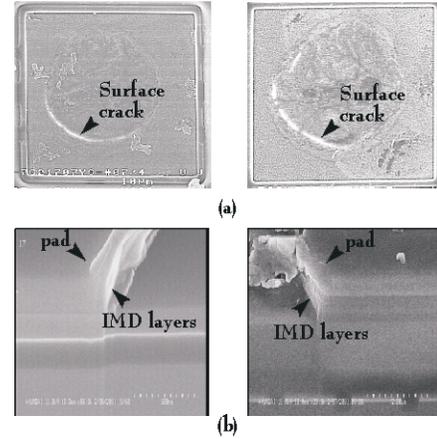


Fig. 11 SEM image of (a) the surface crack on the pad and (b) the fracture of IMD layers after bond pad metal peeling

The fractured shapes of IMD layers are shown in Fig. 11(b). For these SEM images, we have finished FIB works for the precise cross section of fractured region on bonding pad in which the pad metal peeling is occurred.

Because we have known the fact that the maximum plastic strain and the maximum Mises stress are calculated at almost same normalized distance (x/L), in addition, if the fracture of IMD layers occurs in advance of the surface crack, there appear a burr-type fractured shape in bonding pad because of its ductile metal property, we see that the sharply fractured shapes of bonding pad in Fig. 11(b) demonstrates the existence of the surface crack on it before the fracture of IMD layers begins.

The vertically fractured shapes of IMD layers in Fig. 11(b) shows that the surface crack propagates from the pad into the IMD layers. Because the shearing load during the horizontal vibration makes the Mode I type fracture of IMD layers after the surface crack occurs.

Concluding remarks

The effect of the ultrasonic power on the reliability of bonding pad and IMD(Inter Metallic Dielectric) layers has been investigated with numerical analysis and experimental survey. From the results of this study, we find that the the maximum equivalent plastic strain in bonding pad and the maximum Mises stress in IMD layers are induced by ultrasonic power. Furthermore, these values are closely related to the surface crack on the bonding pad and have the significant effect on the fracture of IMD layers and on the propagation of the surface crack into the IMD layers. Therefore careful decision of the ultrasonic power of bonding

machine is necessary to increase the reliability of bonding pad and IMD layers.

Acknowledgments

I. Jeon thanks Dr. Jeong-Tak Moon of M. K. Electronic Co. Ltd. for supplying the experimental material properties of gold wire and Dr. Hyon-Jeong Lee for valuable advice. The wire bonding machine engineers of Hynix semiconductor Inc. is acknowledged for support and helpful discussion.

Appendix A

The calculation of the thermal contact conductance, which can be divided into solid, medium fluid and radiation contact conductance, is needed for analyzing the thermal contact problem. In this paper, we use the results of Tseng[16, 17] straightforwardly.

First of all, we use a equation of solid contact conductance, which is obtained to account for contact interactions under plastic deformations, introduced by Mickic[12] :

$$h_{cs} = 3800k_h R_a^{-0.257} [P/(M + P)]^{0.94} \quad (A-1)$$

where $k_h = 2k_i k_j / (k_i + k_j)$ and $R_a = \sqrt{(R_{ar} + R_{as})}$ are the mean thermal conductivity and arithmetic mean surface roughness, respectively. Furthermore P is the contact pressure, and M is the hardness of the softer material.

In case of the medium fluid conductance for this study, we use a equation achieved by Madhusudona and Fletcher[13] and written as

$$h_{cm} = k_m / \delta_m \quad (A-2)$$

where k_m is the thermal conductivity of the medium and δ_m is the distance between two materials.

Finally, for the radiation contact conductance, we use a equation obtained by Wong[15] as follows

$$h_{cr} = \sigma' [\varepsilon_i \varepsilon_j / (\varepsilon_i + \varepsilon_j - \varepsilon_i \varepsilon_j)] \times [(T_i^4 |_b - T_j^4 |_b) / (T_i |_b - T_j |_b)] \quad (A-3)$$

where σ' is the Stefan-Boltzmann constant, ε_i is the emissivity of the i -th material, T is temperature at absolute scale and the subscript 'b' represents the boundary of contact surface.

Note that all of the thermal contact conductances mentioned above have been calculated with the measured and empirically known data of the materials at which the contact is occurring.

Appendix B

The experimental results of the elastic modulus and the yield stress of gold wire depending upon the temperature are showed in Table B1.

Table B1 The elastic modulus and the yield stress of gold wire

Au wire		
Elastic Modulus(GPa)	Yield Stress(MPa)	Temperature(K)
73.65775	191.6	Room Temp.
73.45181	181.923	323.15
72.43192	168.38	373.15
69.41147	160.635	423.15
66.54793	156.764	473.15
59.02623	141.28	523.15

References

- Melissa Shell-De Guzmán and Michael Mahaney, "The bond shear test: and application for the reduction of common causes of gold ball bond process variation," *Reliability Physics Symposium 1992, 30th annual proceedings, Intenational*, 1992, pp. 251-257.
- Hu, S. J., Lim, G. E. and Foong, K. P., "Study of temperature parameters on the thermosonic gold wire bonding of high-speed CMOS," *IEEE Transaction on Components, Hybrids, and Manufacturing Technology*, Vol. 14, No. 4(1991), pp. 855-858.
- Liang, Z. N., Kuper, F. G. and Chen, M. S., "A concept to relate wire bonding parameters to bondability and ball bond reliability," *Microelectronics Reliability*, Vol. 38, 1998, pp. 1287-1291.
- Shu, W. K., "Fine pitch wire bonding development using statistical design of experiment," *IEEE 1995 Proceedings, 45th Electronic Components and Technology Conference*, 1995, PP. 91-101.
- Tan, Cher, Ming, Er, Eddie, Hua, Younan, and Chai, Vincent, "Failure analysis of bonding pad metal peeling using FIB and AFM," *IEEE Transactions on Components and Packaging Technology, PART I*, Vol. 21, 1998, pp. 585-591.
- Tan, Cher, Ming, Linggajaya, Kaufik, Er, Eddie and Chai, Vincent, "Effect of BOE etching time on wire bonding quality," *IEEE Transactions on Components and Packaging Technology*, Vol. 22, 1999, pp. 551-557.
- Chidambaram, N. V., "A numerical and experimental study of temperature cycle wire bond failure," *Electronic Components and Technology Conference 1991 41st annual Proceedings*, 1991, pp. 877-882.
- Takahasi, Yasuo, Shibamoto, Sigeru and Inoue, Katsunori, "Numerical analysis of the interfacial contact process in wire thermocompression bonding," *IEEE Transactions on Components, Packaging, and Manufacturing Technology, Part A*, Vol. 19, 1996, pp. 213-223.
- Tay, A. A. O. and Seah, B. C., "Finite element simulation of wire looping during wirebonding," *Proceedings of the Advances in Electronic Packaging*, Vol. 1, 1997, pp. 399-406.
- Takahasi, Yasuo, Inoe, Minchinobu and Inoue, Katsunori, "Numerical analysis of fine lead bonding - Effect of pad thickness on interfacial deformation," *IEEE Transactions*

- on *Components and Packaging Technology*, Vol. 22, 1999, pp. 291-298.
11. Takahasi, Yasuo, Inoe, Minchinobu and Inoue, Katsunori, "Numerical analysis of fine lead bonding - Effect of pad mechanical properties on interfacial deformation," *IEEE Transactions on Components and Packaging Technology*, Vol. 22, 1999, pp. 558-566.
 12. Mickic, B. B., "Thermal contact conductance; Theoretical considerations," *Int. J. Heat Mass Transfer*, Vol. 17, 1974, pp. 205-214.
 13. Madhusudana, C. V. and Fletcher, L. S., "Contact heat transfer – The last decade," *AIAA Journal*, Vol. 24, 1986, pp. 510-523.
 14. Lambert, M. A. and Fletcher, L. S., "Review of models for thermal contact conductance of metals," *Journal of Thermophysics and Heat Transfer*, Vol. 11, 1997, pp. 129-140.
 15. Wong, H. Y., "A survey of the thermal conductance of metallic conditions," *ARC Report CP No. 973, Her Majesty's Stationery Office*, London, 1968.
 16. Tseng, Ampere A., "Thermal modeling of roll and strip interface in rolling processes: Part 1 – Review," *Numerical Heat Transfer, Part A*, Vol. 35, 1999, pp. 115-133.
 17. Tseng, Ampere A., "Thermal modeling of roll and strip interface in rolling processes: Part 2 – Simulation," *Numerical Heat Transfer, Part A*, Vol. 35, 1999, pp. 135-154.
 18. Mcmeeking, R. M., "Finite-element formulations for problems of large elastic-plastic deformation," *Int. J. Solids Struct.*, Vol. 11, 1975, pp. 601-616.
 19. Jeon, Insu and Im, Seyoung, "The role of higher order eigenfields in elastic-plastic cracks," *J. Mech. Phys. Solids*, 2001, to be published.
 20. Hetnarski, Richard B., Thermal Stress I, Elsevier Science Publishers B. V.(Netherlands, 1986), pp. 300-389.
 21. Park, Jun and Kwak, Byungman, "Formulation of thermo-mechanical frictional contact based on complementary relations," *Int. J. Solids Struct.*, Vol. 31, 1994, pp. 3217-3231.
 22. Shackelford, James F. et al., CRC materials science and engineering handbook, CRC Press, 1994.
 23. Miner, Douglas F. and Seastone, John B., Handbook of engineering materials, Wiley(New York, 1955).
 24. Minges, Merrill L., Electronic materials handbook, ASM International, 1989.

The mechanical and electrical properties of 6.5 wt.%Si steel for advanced electric components

Young-Ki, Yoon^{a)*}, Jin-Hyeok, Kim^{b)}, and Hi-Seak, Yoon^{a)}

^{a)}Department of Mechanical Engineering, Chonnam National University
300 Yongbong-dong, Buk-gu, Kwangju 500-757, Korea

^{b)}Department of Materials Science and Engineering, Chonnam National University
300 Youngbong-dong, Buk-gu, Kwangju 500-757, Korea

E-mail: ykyoon@chonnam.ac.kr, TEL: 82-62-530-0433, FAX: 82-62-530-1689

Abstract

Fracture behavior and electrical resistance of poly crystals and single crystals of Fe-6.5wt%Si alloy were studied. Electrical resistivities were measured versus temperatures from room temperature to 1000°C. Single crystals were prepared using the Floating Zone (FZ) method, which melts the alloy using a high temperature electron beam in pure argon gas. The single crystals were annealed at 500°C and 700°C respectively and the tensile tests and high-strain-rate deformation tests were performed at room temperature. Disordered body-centered cubic α -iron (A2), ordered bcc α_2 -iron (B2), and ordered hexagonal close-packed α_1 -iron (DO₃) phase were formed in samples annealed at 1000°C/1h, 700 °C/1h, and 500 °C/1h, respectively. The main results are as follows: (1) B2 and A2 phase have elongations of 0.58% and 0.57%, respectively. The DO₃ phase has a lower elongation of 0.49%. It is shown that B2 and A2 phase have better elongations. (2) The electrical resistance of the single crystal is better than that of the polycrystal. (3) Fe-6.5wt.%Si alloy has higher strength at high-strain-rate tensile. SHPB results of polycrystal are twice as high as the static results. (4) From the fractography, the cleavage steps are remarkably reduced in the SHPB test compared with the static test. (5) The resistivity of the alloy is highest at the B2 phase single crystal.

Introduction

In the latter part of the nineteenth century, transformer cores for low-frequency power transformers were made of iron or steel. Because of the large hysteresis losses associated with these materials, the transformers of the day operated at very low efficiencies. At about the turn of the century it was discovered that the addition of a little silicon greatly increased the permeability of low-carbon steel and substantially reduced the hysteresis loss. It was found that the improvement in hysteresis properties came from the fact that silicon increases the electrical resistivity of steel and thereby reduces the eddy current losses. Until now, silicon iron containing about 3 wt.% silicon is widely used as an electric sheet for core materials of electric machines [1,2].

However, since it is generally known that iron loss decreases with the increase of silicon content in silicon iron alloy and can take a minimum of 6.5 wt.% silicon content, researchers realize the characteristics of silicon iron. It is well known that heat treatment in a magnetic field has been found effective for iron-silicon alloys between two percent and ten percent silicon, the highest maximum permeability being obtained at about 6.5 percent silicon [3-5]. Iron-based alloys

containing about 6.5-percent silicon have a potential application in magnetic devices due to their high electrical resistivity, very low magnetostriction, and low magnetocrystalline anisotropy. In addition, these high-silicon alloys have been shown to be more responsive to magnetic annealing than alloys with lower silicon content. The core material exhibits both low iron losses in the high frequency range, resulting in the increment of the utility life for an electric component. However, it is also well known that the improvement of the cold-workability of high-silicon alloy is extremely difficult. It has been found that three structurally different ordered phases; exist DO₃, B2, and A2 structure [6,7].

The order-disorder phenomenon and the resulting phase diagram of higher silicon-iron alloys have been studied by a number of researchers. However, the effect on the mechanical and electrical properties of various phase for Fe-6.5wt.%Si single crystal have scarcely been reported.

Resistivity is the capacity for or tendency toward resistance shown electrical properties on a material. Therefore, in this paper, the resistivity is measured to determine the electrical characteristics of the alloys. In addition, the available alloy phase is proposed by comparing mechanical properties and electrical properties.

Preparation of specimen and experiments

The alloys were prepared by melting electrolytic iron (99.9 percent purity) and metallic silicon (98 percent purity) in a vacuum induction furnace, and then poured into a square ingot mold. The mother ingots of FeSi (Fe-6.5wt.%Si) alloys were prepared by melting high purity Fe and Si in a plasma arc furnace. Rods with dimensions of 10 mm in diameter and 100 mm long were cut from the ingots by spark machinery. Crystals containing a single set of unidirectionally aligned lamellae were grown from these ingots using the floating zone method. Crystal growth was carried out using a single crystal growing apparatus (NEC SC-35HD, NEC machinery corporation, Tokyo, Japan) with an optical heat source at a growth rate of 5 mm/h under a high purity argon gas flow [8,9].

High strain tensile and static tensile dog-bone type specimens with a gauge length dimensions of 2×2×5 mm were fabricated from the bulk crystals by spark machining, and were subsequently, mechanically polished on emery paper, and then electrolytically polished in a solution of 10% HClO₄ and 90 CH₃COOH at 8°C and 15V for 5min to remove surface damage. The crystals were then cooled after homogenization at 1000 °C for 48h and subsequently annealed at 1000 °C for 1h, and continuously annealed at 700 °C or 500 °C for 1h.

Formation of crystalline phases after the annealing process was characterized by an x-ray diffractometer (XRD) (DMAX/1200, RIGAKU, Japan) using θ - 2θ scans. X-ray θ - 2θ diffraction patterns were obtained from the samples annealed at various temperatures of 1000 °C (A2), 700 °C (B2), and 500 °C (DO₃), and room temperature. A2, B2 and polycrystal phase alloys are *bcc* type alloys. However, DO₃ alloy has *hcp* crystalline [10].

The static tensile tests were performed at room temperature using the TOYO-BALDWIN (Japan) testing machine. The high-strain-rate tensile tests were performed using the tensile split Hopkinson bar test machine (HanKook Machinery, co., Korea). A specimen is connected to Inconel bars using the specimen holders made by the same alloy. The striker bar is accelerated by compressed air and creates a tensile wave when hitting the stop at the end of the input bar. The strain gauges mounted on the bars measure the strain of the incident, reflected waves, and transmitted waves. The strain gauges in each bar are connected to a Wheatstone bridge in such a way that signals from bending waves are suppressed. The signals are recorded by a data acquisition card (Model: GageScope 8012A, GaGe, USA). High-speed optical sensors (Model: LS-5000, KEYENCE, United Kingdom) measure the speed of the striker bar [11].

The Keithley 2400 Series SourceMeter is used for sourcing the current (I) and measuring the voltage (V) of each sample with different phases. The sample to check the voltage is mounted on the holder. The sample is connected with 99.99% platinum wire (Goodfellow, England) to the SourceMeter. The source current (I_{src}) is maintained at +100.00 μ A definitely. Resistivity is measured by the potentiometric method. Figure 1 shows the design of the measuring system for the resistivity.

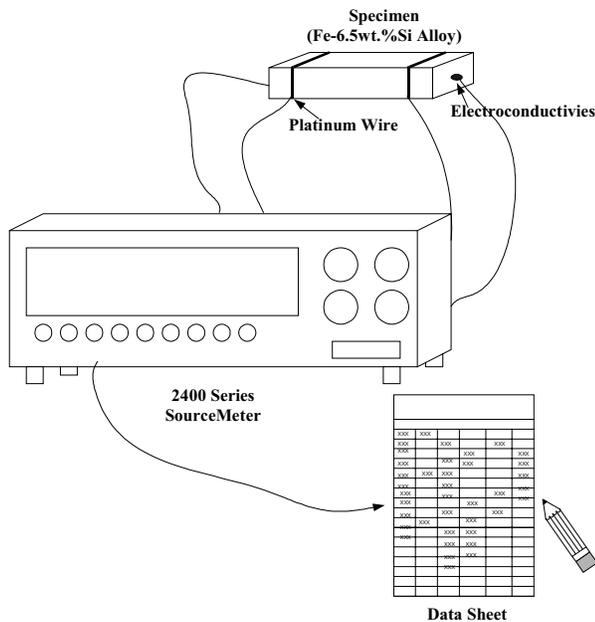


Fig. 1 Schematic diagram of the system for measuring a resistivity of Fe-6.5wt.%Si polycrystal and single crystal at room temperature.

Results and discussion

Figure 2 shows the static tensile test results of Fe-6.5wt.%Si polycrystal and A2, B2, and DO₃ phases of single crystals at room temperature. The polycrystal eliminated an internal residual stress has 252MPa of the tensile fracture strength and 0.05% elongation. Therefore, polycrystal shows the curve graph of brittleness.

After the solution heat treatment, a specimen is annealed again and subsequently, quenched in the water for the A2 phase. This phase specimen shows 671MPa of fracture strength and 0.57% elongation. The specimen improved in strength and elongation compared to the polycrystal. DO₃ phase single crystal has 595MPa of fracture strength and 0.49% elongation. This phase single crystal is poor in strength and elongation to A2 phase single crystal. B2 phase single crystal has 528MPa of strength and 0.58% elongation. These results are like the A2 phase single crystal in the mechanical properties.

Figure 3 shows the high strain rate tensile test results of Fe-6.5wt.%Si polycrystal and single crystal with DO₃ phase using the SHPB test method at room temperature. From the viewpoint of ductility and strength, attention should be paid to the stress-strain curves deformed at various alloy phases. It appears that the single crystal is higher in strength than the polycrystal. The polycrystal and single crystal show 560MPa and 850MPa strengths, respectively. It is also revealed that single crystal has higher strength than polycrystal as shown in the static tensile test. The results show that the strength of the single crystal increases one-third higher than the polycrystal. This indicates that the single crystal of silicon iron is better than the polycrystal in strength and elongation on the static and high strain rate tensile tests.

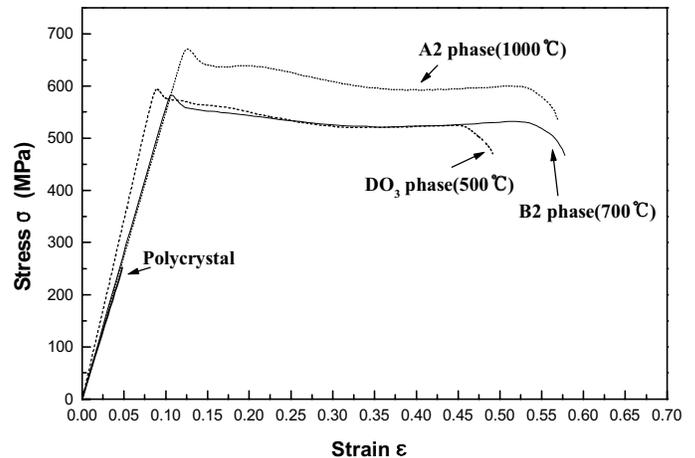


Fig. 2 The tensile test results of Fe-6.5wt.%Si polycrystal, α (A2), α_1 (DO₃), and α_2 (B2) single crystal specimens under room temperature.

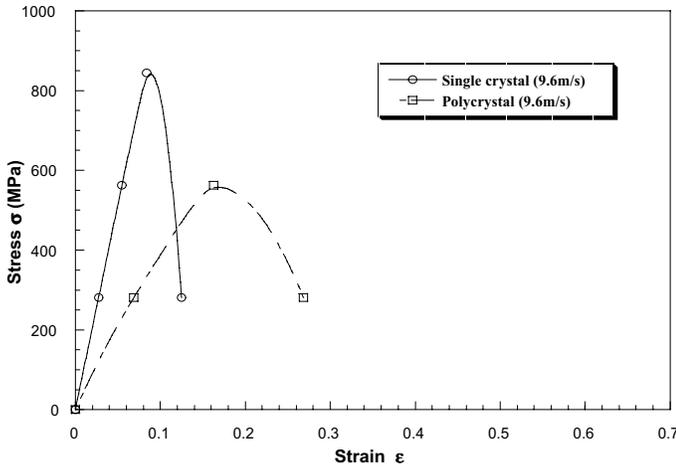


Fig. 3 The high strain rate tensile test results of Fe-6.5wt.%Si polycrystal, and α_1 (DO_3) single crystal specimens under room temperature.

It is well known that resistivity changes with ordering. Therefore, resistivity (ρ , $\mu\Omega\text{-cm}$) was then measured for specimens subjected to heat-treatment and crystal phases of the alloys. The electrical resistance is proportional to the length of the wire and inversely proportional to the cross-sectional area and thus is not an intrinsic property of the material. Therefore, it is appropriate to focus our attention on the resistance of a sample of unit length and unit cross-sectional area. The detail length and area of the samples are applied to the electrical resistivity (ρ) formula, which is expressed as length (L), area (A), and electrical resistance (R) in ohms when the current (I) is expressed in amperes and the voltage (V) is expressed in volts.

The results are shown in Table 1 and Fig. 4. The table and figure clearly demonstrate that resistivity drops sharply at polycrystal and α_1 (DO_3) phase which was annealed at 500°C . And the α (A_2) phase which annealed at 700°C has a high resistivity. These results strongly suggest that a structural change, which is probably the formation of an ordered structure, takes place at 500°C and 700°C .

Table 1 Comparison of measured values for the materials. Each absolute value is the largest of those obtained for various specimens.

Specimen Phase	Voltage, V (mV)	Resistivity, ρ ($\mu\Omega\text{-cm}$)
Polycrystal	300	1.841×10^{-4}
Single crystal, α_1 (DO_3)	340	2.466×10^{-4}
Single crystal, α (A_2)	400	3.542×10^{-4}
Single crystal, α_2 (B_2)	780	6.567×10^{-4}

Figure 5 shows the scanned electron micrographs of fractured surface of Fe-6.5wt.%Si polycrystal and single crystal specimen in static tensile test and high strain rate tensile test. Fracture surfaces of the alloys in the static tensile test- (a) through (d) - and in the high speed tensile test-(e) through (f) are presented. Figure 5 (a) is a fracture surface of a polycrystal. Fractured appearances for brittle materials are shown river pattern, cleavage step, tilt boundary, and twist boundary. Figure 5 (b) shows fracture surface of a single crystal with α (A_2) phase. It shows straight cracks parallel to fracture surfaces. Figure 5 (c) indicates fracture surface of a single crystal with α_1 (DO_3) phase. It also shows straight cracks similar with fig. 5 (b). A transverse straight crack, which is shown in the brittle alloys, also is shown. Figure 5 (d) is fractured surface of a single crystal with α_2 (B_2) phase. There are also cleavage type fractures, but, no transverse straight cracks shown in fig. 5 (b) and (c). In the B_2 phase, some herringbone structures, generally observed in the absence of twinning and cleavage-like fracture of normally ductile materials are shown [12,13].

From these observations, one may conclude that polycrystals have a lot of cleavage patterns which mean the brittleness of the alloy and B_2 phase single crystal annealed at 700°C has more ductile fracture patterns than other phases of the single crystal.

Figure 5 (e) demonstrates a fracture surface of a polycrystal at the high strain rate tensile test by SHPB method. There are some cleavage steps. However, the steps are rare compared with the static tensile test. Figure 5 (f) shows a fracture surface of single crystal at the high strain rate tensile test. There are small river patterns without the cleavage steps. The transverse straight cracks are not shown and the cleavage fracture patterns are reduced in these photos.

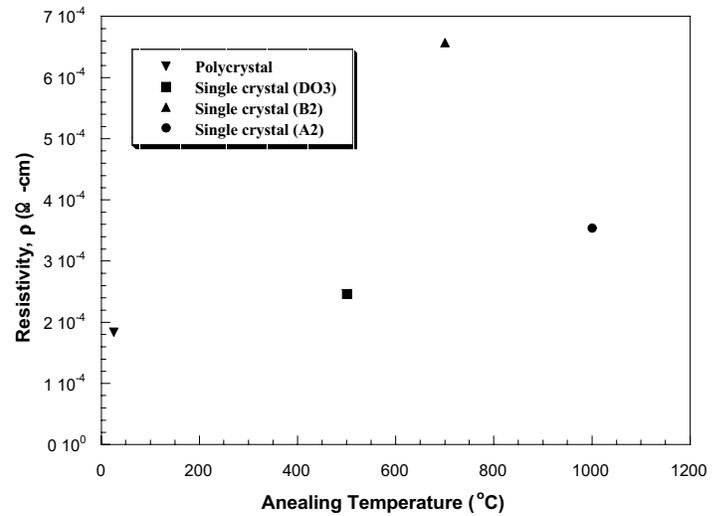
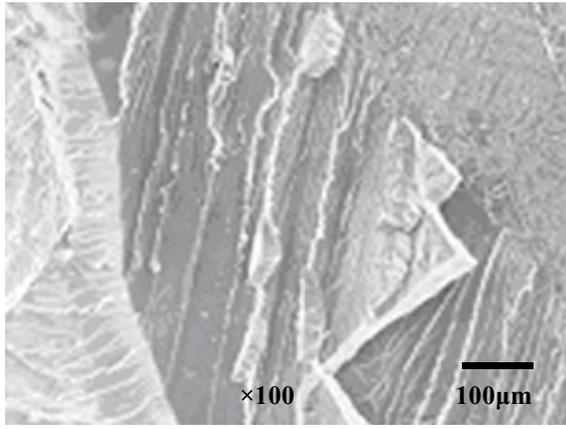
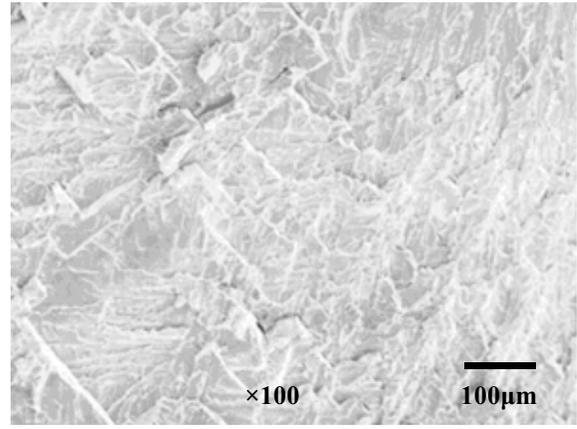


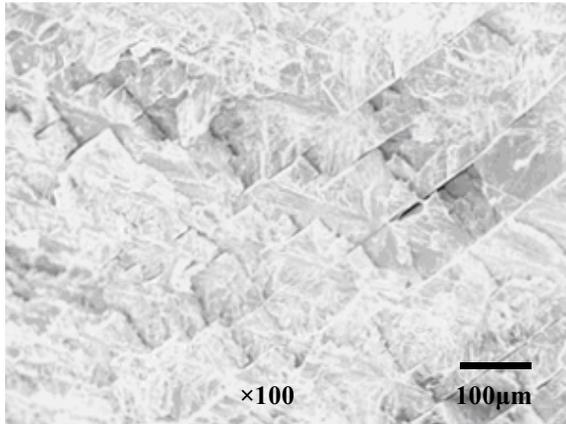
Fig. 4 The resistivity (ρ) of Fe-6.5wt.%Si polycrystal, α (A_2), α_1 (DO_3), and α_2 (B_2) single crystal specimens under room temperature.



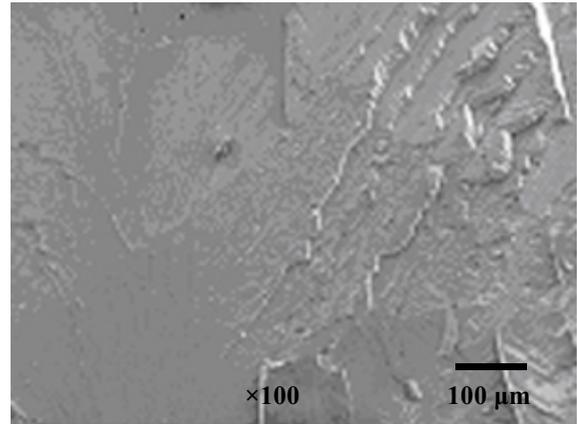
(a)



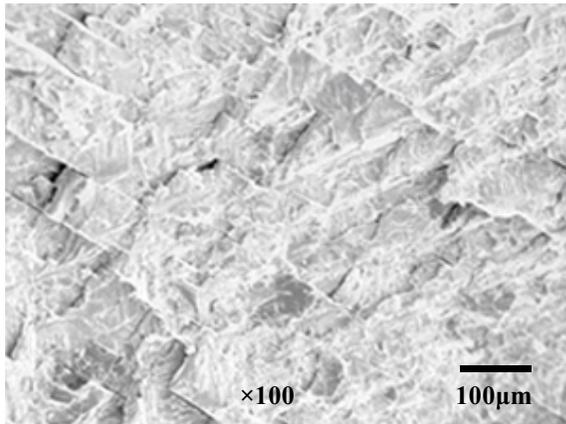
(d)



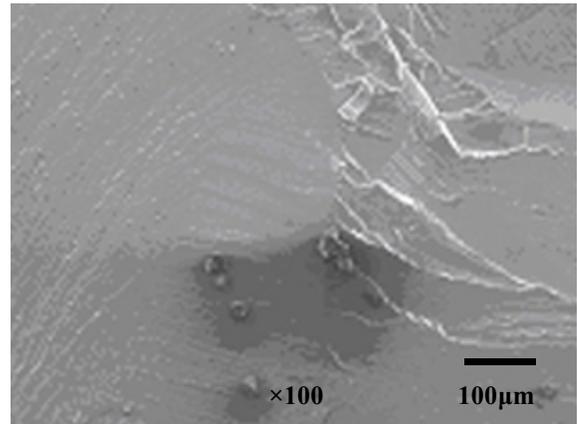
(b)



(e)



(c)



(f)

Fig. 4 Fracture surfaces of Fe-6.5wt.%Si in the static tensile test- (a) through (d) - and fracture surfaces in the high speed tensile test-(e) through (f). (a) Fracture surface of a polycrystal. There are cleavage steps showing brittleness. (b) Fracture surface of a single crystal with α (A2) phase. It shows straight cracks parallel to fracture surfaces. (c) Fracture surface of a single crystal with α_1 (DO₃) phase. It also shows straight cracks similar with (b). (d) Fracture surface of a single crystal with α_2 (B2) phase. There are cleavage type fractures. However, there are no transverse straight cracks shown in fig. (b) and (c). (e) Fracture surface of a polycrystal. There are some cleavage steps. However, the steps are rare compared with the static tensile test. (f) Fracture surface of a single crystal. There are small river patterns without the cleavage steps.

Conclusions

Mechanical properties and fractographs of Fe-6.5wt.%Si single crystals and polycrystals were investigated at the static and high strain tensile mode. In addition, the electrical property of the alloy was also observed.

1) Single crystal has a good elongation compared with polycrystal. It was found that α_1 (DO₃) and α_2 (B2) are backward in the strength of α (A2) phase single crystals. However, it is revealed that B2 phase crystal has a better elongation to DO₃ phase crystal.

2) The mechanical property of alloy in the high-strain-rate tensile test indicates that the strength of the alloys is higher than those of the static tensile test.

3) Cleavage fractures are reduced under the condition of higher speed tensile mode. In addition, the short transverse straight cracks come out on the surface.

4) Resistivity was measured to define the electrical property of Fe-6.5wt.%Si. In these results, α_2 (B2) phase annealed at 700 °C. It has the highest resistivity compared with other phase materials.

5) From results, α_2 (B2) phase single crystal is suggested as the suitable iron steel for advanced electric component for the reason of high strength, elongation, and resistivity as compared with those of other phases.

Acknowledgments

This work was supported by the Brain Korea 21 Project. The authors also extend their appreciation to Prof. Y.Umakoshi and Dr. H.Y.Yasuda of Osaka University, Japan. They provided a support to the manufacture of the Fe-6.5 wt.%Si alloy ingot and single crystal.

References

1. Goss, N. P., "Electrical Sheet and Method and Apparatus for its Manufacture and Test," *US Patent*, No. 1,965,559 (1934), pp. 1-11.
2. Kim, J. C. *et al*, "Effects of Rolling Conditions on Grain Orientation and Magnetic Properties of Thin-Gauged 3% Si-Fe Sheets", *Scripta Mater.*, Vol. 38, No. 9 (1998), pp. 1405-1409.
3. Goertz, M, "Iron-Silicon Alloys Heat Treated in a Magnetic Field," *J. Appl. Phys.*, Vol. 22, No. 7 (1951), pp.964-965.
4. Tanaka, Y. *et al*, "Magnetic properties of 6.5%Si-Fe sheet and its applications," *J.Magn.Mater.*, Vol. 83, (1987), pp. 375-376.
5. Ninomiya, H. *et al*, "Magnetostriction and applications of 6.5%Si steel sheet," *J.Appl.Phys.*, Vol. 69, No. 8 (1991), pp. 5358-5360.
6. Kubaschewski, O, *Iron Phase Diagrams*, Springer (Berlin, 1982), pp. 136-139.
7. Heikinheimo, E. *et al*, "Interdiffusion in Ordered and Disordered Fe(Si) Solid Solution," *J.Magn.Mater.*, Vol. 38, No. 8 (1991), pp. 1229-1235.
8. Glebovsky, V. G. *et al*, "Growing Techniques and Structure of Niobium Bicrystals," *J.Crystal Growth*, Vol. 59 (1982), pp. 450-454.
9. Kadeckova, S. *et al*, "Stabilization of floating liquid zone in preparation of Fe-Si alloy single crystals," *Brit. J. Appl. Phys.*, Vol. 14 (1963), pp. 927.
10. Yoon, Y. K. *et al*, "Effect of Annealing on the Mechanical Properties of Fe-6.5wt.%Si Alloy," *TRANS. KSME (in Korean) A.*, Vol. 24, No.12 (2000), pp. 2909-2916.
11. Yoon, Y. K. *et al*, "High-Strain-Rate Deformation of Fe-6.5wt.%Si Alloys using a Split Hopkinson Pressure Bar Technique," *TRANS. KSME (in Korean) A.*, Vol. 25, No.7 (2001), pp. 1073-1081.
12. Pittinato, G. P. *et al*, *SEM/TEM Fractography Handbook*, Metals and Ceramics Information Center (USA, 1975), pp. 25-57.
13. Lynch, S. P. *et al*, "Herringbone patterns on fracture surfaces," *Scripta Metall.*, Vol. 20 (1986), pp. 1067-1072.

Circuit Modeling Technique of Electronic Package Considering S-parameters Measurement Environments

Yong-Ju Kim*, Kwang-Seong Choi**, Young-Suk Suh*, and Hwa-jung Kim*

*Module Development Team, Hynix Semiconductors

San 136-1, Ami-ri, Bubal-eup, Ichon-si, kyoungki-do, 467-701 Korea

Phone:82-31-630-4453, Fax:82-31-630-2338, E-mail : yongju.kim@hynix.com

** Optical Module Packaging Team

Electronics and Telecommunications Research Institute

Phone : 82-42-860-6033, Fax: 82-42-860-6836

E-mail: kschoi@etri.re.kr

Abstract

Generally, In order to extract electrical circuit parameters of package, specific test fixtures composed of short, open, and thru patterns are required. However, electrical parasitic of the test fixtures makes difficult to extract accurate circuit parameters of the package. In addition to the values of the parameters have many different according to the electrical configurations of adjacent pins as like floating, dc biasing, and applying RF signal. In this paper, we presented a new modeling technique of electronic package considering measurement environments. Almost electrical parasitic components effect on capacitance and inductance of the package are considered in the proposed modeling technique. The modeling technique is verified through comparison between the measured s-parameter by VNA and the results by AC analysis.

I. Introduction

In the high-speed digital system and RF system, the electrical parasitics of the electronic package can significantly limit the performance of the system. The inductance of the package induces the simultaneous switching noises (SSN) on the power bus line of the system. The transmission line behaviors of the package produce the crosstalk, reflection and EMI. Management of the electrical noises and timing margin due to these noises is major topic in design of high-speed systems. Especially, as operating frequency increase, accuracy of modeling and its parameter are very essential factors to design of the high-performance system.

There are many approaches for modeling of electronic package through s-parameters measurement by VNA [1]-[4]. C. T. Tsau have been proposed the measurement of self-inductance of package leads from one-port s-parameters measurement for test package with electrically short-path. C [1][2]. B. Y. Young have measured the self and mutual inductance of packages with more than 120 pins from s-parameter for two-port network composed of coupled leads terminated in short circuit[3][4]. T.Tsau have used test package that all pins electrically float except except probed pins for capacitance[2].

As shown above, in order to extract electrical circuit parameters of package, specific test fixtures composed of short and open patterns are required. In order to extract electrical parameters of 48-pin LQFPs, we also prepared a test board contained test packages with electrically short, open, and thru-path. In the case of short-patterns, all package leads are connected to a metal plate, which is intentionally inserted

into the inside of package, and the most of package leads are shorted to ground through via of PCB. In this situation, the accurate measurement of the package inductance is very difficult because of the parasitic inductance of unknown current return path and magnetic coupling between package lead and the return path. Moreover, the measured capacitance on the test fixture includes values of capacitance not only between package leads but also between package leads and the plate of board. In this paper, we will present package modeling and its parameters extraction technology taking into account for the electrical parasitic parameters of the test fixture and electrical interaction between adjacent pins.

In order to extract the accurate electrical parameters of the package, we modeled the test fixture to lumped circuit network considering all current paths existed in the fixture and their electric and magnetic interactions. Initial model parameters of the circuit are obtained by using static magnetic and electric simulator. The s-parameters of the network applied initial model parameters are obtained by simulation through HSPICE. And then final model parameters are computed by minimization of difference between the measured s-parameters by VNA and the simulated s-parameters.

Fabrication and Measurement of Test Pattern

Test fixture with test packages, 48-pin LQFP, soldered on the top layer of double side PCB is prepared for the s-parameter measurement and the circuit modeling of the package. The test vehicle has three electrically different interconnects configurations denoted by open-path, short-path, thru-path, respectively. In Fig. 1, the simple schematic diagram of the fixture is described and the cross-sectional view of the test fixture is shown Fig. 2. As shown in Fig. 1 and Fig. 2, all package lead frames except several pairs of lead frames allocated for s-parameter measurement are shorted to ground plane, the bottom layer of the PCB, through via and their another ends are connected to the paddle (metal plate) by wire bonding. And the lead frames for s-parameter measurement are connected to probing pad formed in the bottom layer. The test packages with three electrically different interconnects configurations, open-path, short-path, and thru-path, are obtained by wire bonding technology. In the case of test patterns with short-path, two types of packages are prepared. Fig. 1(c) is a test package to measure for electrical characteristic when adjacent pins work on current return path. While Fig. 1(d) is a test package to characterize electrical

characteristic when the paddle, counterpart pins of probed pin, and the ground plane effects on current return paths.

The s-parameters of the prepared test fixture are measured by using Cascade Microtech probe station, 50Ω coplanar microwave probe and HP8720C network analyzer after a two-port SLOT(short, open, load, and through) calibration for de-embedding the parasitics of cable and probe(S-G, G-S).

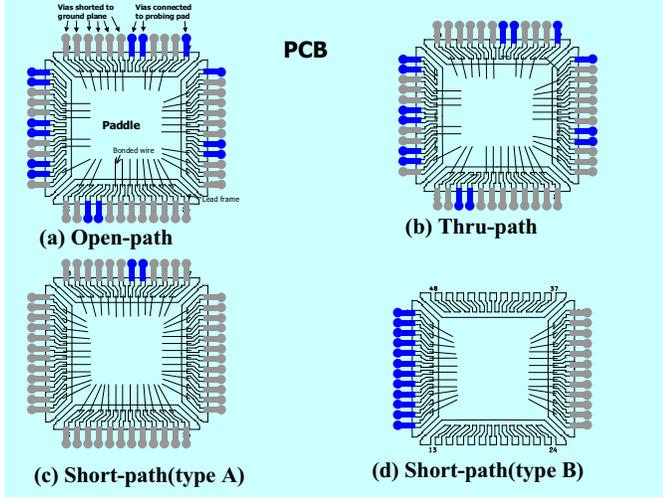


Fig. 1 Top view of the test fixture

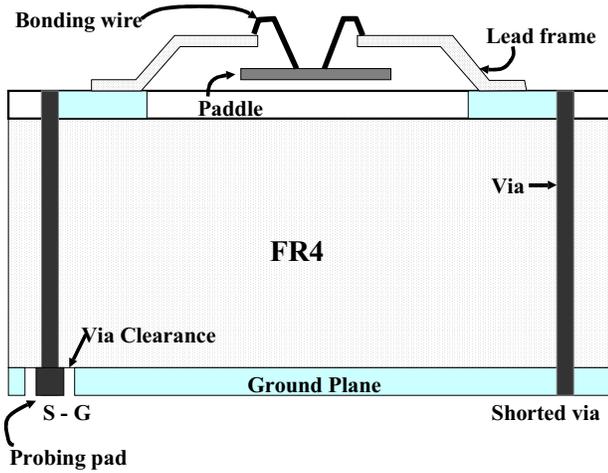


Fig. 2 Cross-sectional view of the test fixture

Circuit Modeling of test environment

For accurate circuit modeling of the measurement environment, the test fixture were divided into three blocks as shown in Fig. 4. They are probing pads, lead-frames and bonding wires, and the modeling of paddle. Three different modeling approaches are applied on each blocks, respectively. In this section, a detailed description of the modeling approach for each blocks are presented.

A. Modeling of probing pad

For circuit modeling of the probing pads, two kinds of test patterns with different electrical configuration, short-path and open-path, patterns are included in the test fixture. In Fig. 4, a

brief description of the test pattern is given. As mentioned section II, the probing pad is through-hole type via and via land is used as landing pad for GS type microwave probe.

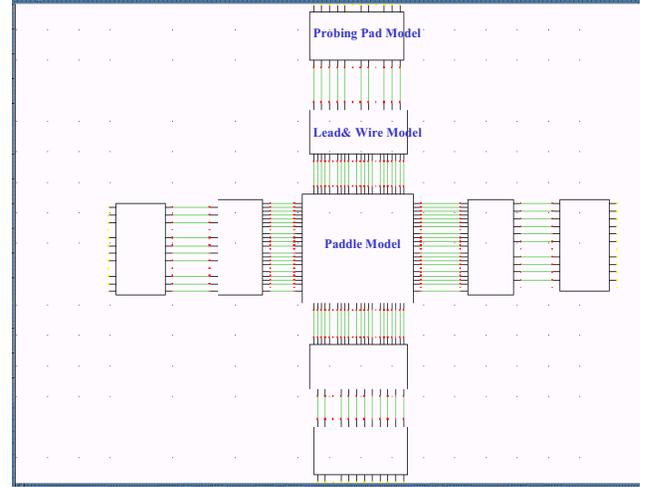


Fig. 3 Block diagram for modeling of the test fixture.

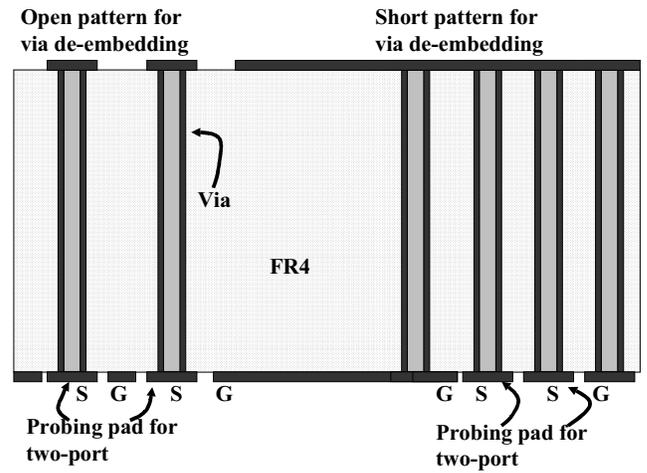


Fig. 4 De-embedding pattern of probing pads

The probing pad is modeled by using simple lumped model shown in Fig. 5. In order to determine values of the elements in the equivalent circuits for probing pad, the lumped model assumption is used. In the case of the test pattern terminated with open-circuits, series impedance of the equivalent circuits can be ignored in range of low frequency, $f \ll 1/2\pi\sqrt{LC}$. In order to obtain values of capacitance of the equivalent circuits, the measured s-parameters have to be converted into two-port y-parameters. The relationship between the measured two-port s-parameters and two-port y-parameters are

$$Y_{11} = \frac{1}{Z_0} \frac{(1 - S_{11})(1 + S_{22}) + S_{12}S_{21}}{(1 + S_{11})(1 + S_{22}) - S_{12}S_{21}} \quad (1)$$

$$Y_{12} = \frac{1}{Z_0} \frac{-S_{12}}{(1 + S_{11})(1 + S_{22}) - S_{12}S_{21}} \quad (2)$$

From lumped approximation, the self-capacitance and mutual capacitance are directly calculated from (1) and (2) as follows

$$C(f) = \frac{1}{2\pi f Z_0} \text{Im} \left[\frac{(1 - S_{11})(1 + S_{22}) + S_{12}S_{21}}{(1 + S_{11})(1 + S_{22}) - S_{12}S_{21}} \right] \quad (3)$$

$$C_m(f) = \frac{1}{2\pi f Z_0} \text{Im} \left[\frac{-S_{12}}{(1 + S_{11})(1 + S_{22}) - S_{12}S_{21}} \right] \quad (4)$$

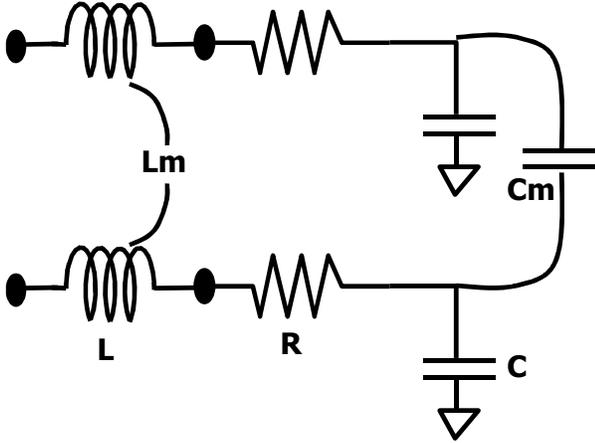


Fig 5. Equivalent circuit for the probing via.

While, in the case of the test pattern terminated with short-circuits, parallel admittance of the equivalent circuits can be ignored in range of low frequency, $f \ll 1/2\pi\sqrt{LC}$ too. Under this assumption, self-inductance and mutual inductance are obtained by the relationship between the measured two-port s-parameters and two-port z-parameters as follow equations,

$$\frac{Z_{11}}{Z_0} = \frac{(1 + S_{11})(1 - S_{22}) + S_{12}S_{21}}{(1 - S_{11})(1 - S_{22}) - S_{12}S_{21}} \quad (5)$$

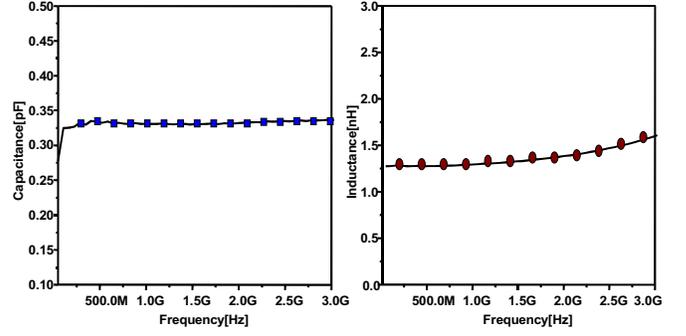
$$\frac{Z_{12}}{Z_0} = \frac{2S_{12}}{(1 - S_{11})(1 - S_{22}) - S_{12}S_{21}} \quad (6)$$

$$L(f) = \frac{Z_0}{2\pi f} \text{Im} \left[\frac{(1 + S_{11})(1 - S_{22}) + S_{12}S_{21}}{(1 - S_{11})(1 - S_{22}) - S_{12}S_{21}} \right] \quad (7)$$

$$L_m = \frac{Z_0}{2\pi f} \text{Im} \left[\frac{2S_{12}}{(1 - S_{11})(1 - S_{22}) - S_{12}S_{21}} \right] \quad (8)$$

$$R(f) = Z_0 \text{Re} \left[\frac{(1 + S_{11})(1 - S_{22}) + S_{12}S_{21}}{(1 - S_{11})(1 - S_{22}) - S_{12}S_{21}} \right] \quad (9)$$

Capacitance and inductance of the equivalent circuit obtained by lumped model approximation are presented Fig. 6.



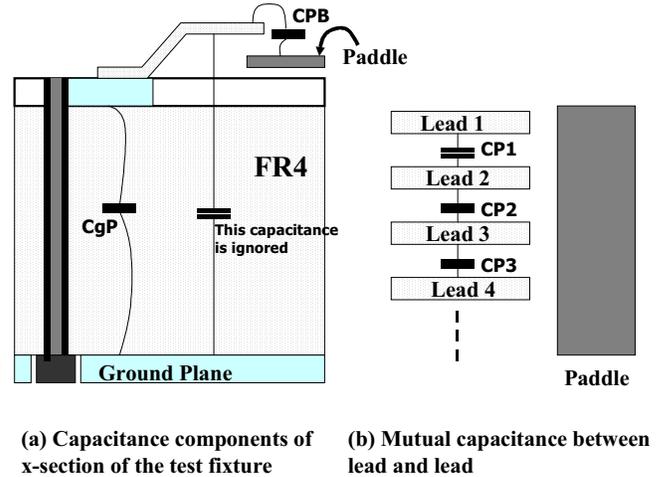
(a) Capacitance of via

(b) Inductance of via

Fig. 6 Capacitance and inductance of probing via

B. Modeling of the package lead-frames

The measurement results of the package mounted on the test fixture vary according to electrical configurations of the neighbor pins. In addition to, various parasitic electrical components due to geometry of the test fixture make more difficult to obtain accurate circuit parameters of the package. In order to overcome this situation, in this paper all parasitic components existed in the test fixture are considered. In Fig.7, brief diagram described parasitic elements for capacitance is given. As shown in Fig. 7, lead-to-lead capacitance, lead-to-PCB plane capacitance, and lead-to-paddle capacitance are taken into account. Each capacitance is obtained by static electric filed simulation. Later, these values may be modified though optimization using measurement results of the test fixture.



(a) Capacitance components of x-section of the test fixture

(b) Mutual capacitance between lead and lead

Fig. 7 Capacitance components for circuit modeling of the leads

Loop inductance is a function of current return path. Since various return paths in the test fixture according to electrical configurations of pins, full pin model of the package is required to obtain partial inductance of lead frame. In this paper, we model all return paths can be existed in the test fixture. Graphical description of the return paths is given Fig. 8 and Fig. 9. As shown in Fig. 9, static current distribution is

assumed. Values of inductance of each current path are obtained by EM-simulation. Finally, circuit model of the package is shown in Fig. 10.

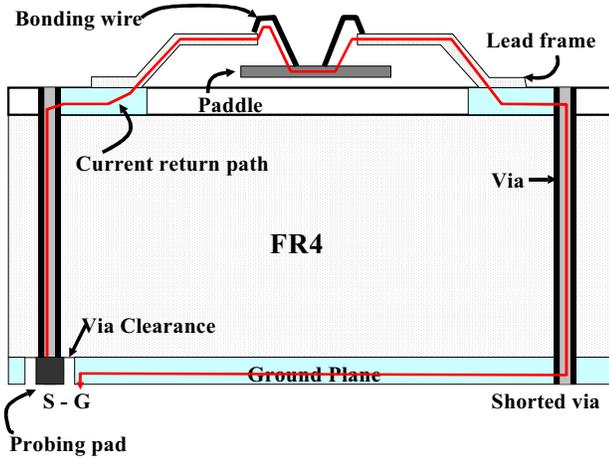


Fig. 8 Current return path for inductance modeling (cross-sectional view).

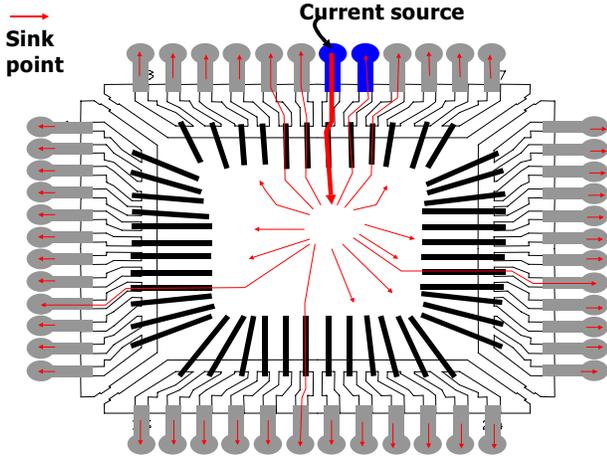


Fig. 9 Current return path for inductance modeling (top view).

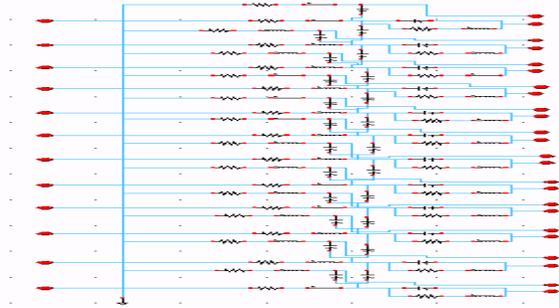


Fig. 10 Circuit model of the package.

C. Modeling of the paddle

In order to construct electrically short-path in the test fixture, a paddle is inserted in a LQPF package. In Fig. 8, a cross sectional view is shown. Two conductors, the ground plane of the PCB and the paddle in the test package, forms micro-strip transmission line. Dielectric materials between two

conductors are stacked in sequence of FR4, air, and EMC. Their dielectric constants are 4.4, 1, and 3.9, respectively.

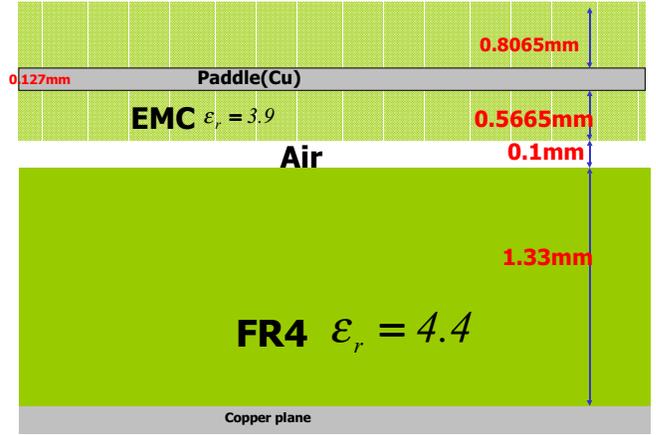


Fig. 11. Cross-sectional view of the test fixture for paddle modeling.

The paddle is divided into a number of smaller rectangular tiles as shown in Fig. 12. This tile is modeled by the w-element of HSPICE. Distribute capacitance of the tile is computed static-electric filed solver. In Fig. 13, simulation window and boundary conditions used in EM-simulations is described. In the case of tiles of the paddle edge, only one face, left or right, is set to Neumann boundary condition, others are Dirichlet boundary. While, in rest tiles, left and right faces are set to Neumann boundary and top and bottom faces are applied Dirichlet boundary. Inductance of the tile is calculated under Quasi-TEM approximations as like

$$L = \frac{l}{c_0^2 C} \quad (10)$$

Other parameters of the tile can be computed as[5]:

$$R_d = \frac{2}{\sigma_c t} \quad (11)$$

$$R_s = \frac{2 \left(\sqrt{\frac{\pi f \mu_0}{\sigma_c}} - R_d \right)}{\sqrt{f}} \quad (12)$$

$$G_s = C \tan(\delta) \quad (13)$$

In the above equations, μ_0 is the permeability of free space. The parameters, R_d and R_s , and G_s , are resistance terms in W-elements of HSPICE.

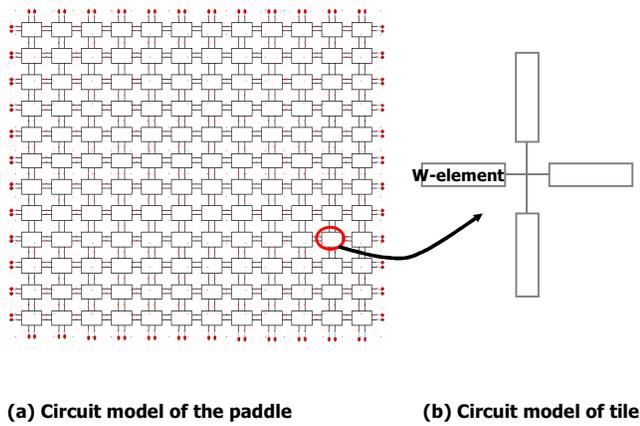


Fig 12. PEEC modeling of the paddle of the package.

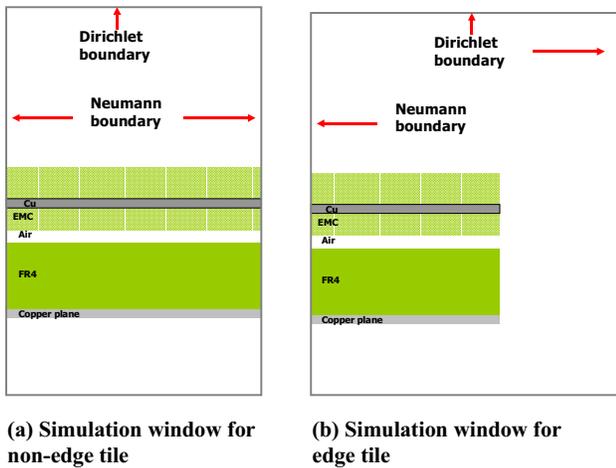


Fig 13. Simulation windows to compute capacitance of tiles.

Results and Discussions

For correlation between the measured s-parameters and these of AC analysis using proposed circuit model of the test fixture, the simulated s-parameters are compared with the measured data for all test pattern configurations shown in Fig.1. If difference between two data is detected, we will modify circuit model parameter through minimization of error. The minimization algorithm used in here is genetic algorithm.

In this section, we selected a pin every test packages shown in Fig. 1. Imaginary part of S11 of test pattern with electrically open-path is shown in Fig. 14. The s-parameter obtained by AC analysis is good agreement with that of measurement. Fig. 15 shows results of a test pattern shown in Fig. 1(c). Main current path of this pattern is neighbor pins and mutual inductance reduce value of loop inductance. Therefore electrical length of the test pattern is very short and the test pattern can be modeled by lumped model approximation. In Fig. 16, imaginary part of the s-parameters of the test pattern with short-path type B is shown as a function of frequency. This pattern has long current path that formed from probing pin through the paddle and leads in counter part of probing pin to ground via. As shown in Fig. 16,

a few of resonance peaks due to large loop inductance are founded. And the proposed model explained this situation.

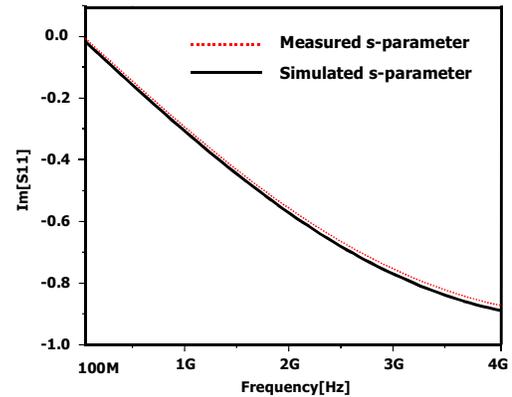


Fig. 14 Comparison with the measured s-parameters and the simulated s-parameters.

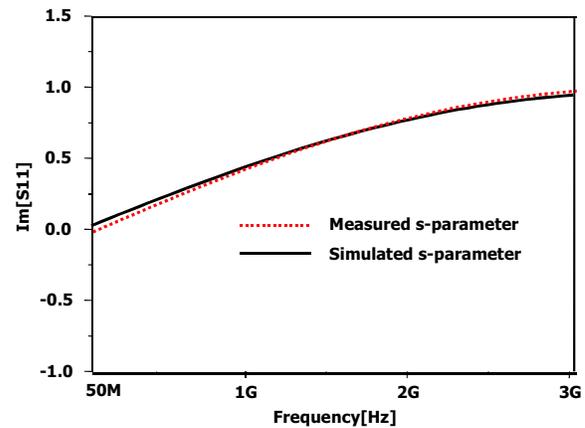


Fig. 15 S-parameter of the test pattern with electrically short-path.

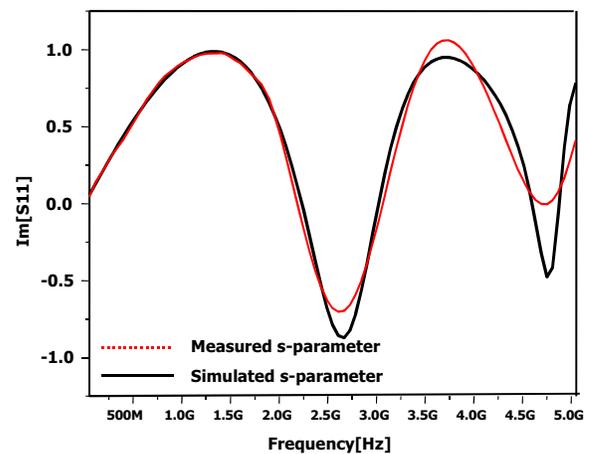


Fig. 16 S-parameter of test pattern with short-path(B)

Conclusions

The circuit modeling technique for test fixture to measure electrical characteristic of electronic packages is presented. In the proposed model, almost parasitic component including electromagnetic coupling and current return paths generated general test fixture is considered. These components are modeled under static assumption. The circuit model of the test fixture gives a good explanation of electrical characteristic presented by s-parameter measurements. This technique is very useful for modeling of packages mounted on high-performance board.

References

1. C. T. Tsai and W. Y. Yip, "An Experimental Technique for Full Package Inductance Matrix characterization," *IEEE Trans. Comp., Packag., Manufact. Technol., part B*, vol. 19, no. 2, pp. 338-343, May 1996.
2. C. T. Tsai, "Package Inductance Characterization at High Frequencies", *IEEE Trans. Comp., Packag., Manufact. Technol., part B*, vol. 17, no. 2, pp. 175-181, May 1994.
3. B. Young and A. K. Sparkman, "Measurement of Package Inductance and Capacitance Matrices," *IEEE Trans. Comp., Packag., Manufact. Technol., part B*, vol. 19, no. 1, pp. 225-229, Feb. 1996.
4. B. Young, "Return Path Inductance in Measurements of Package Inductance Matrices," *IEEE Trans., Comp., Packag., Manufact. Technol., part B*, vol. 20, no. 1, pp. 50-55, Feb. 1997.
5. J.H. Kim and M. Swaminathan, "Modeling of Irregular Spaced Power Distribution Planes Using Transmission Matrix Method," *IEEE Trans Advanced Packaging*, Vol. 24, No. 3, pp. 334-346, Aug. 2001